 doi: 10.1111/j.1365-246X.2008.03763.x

Shear and compressional velocity models of the mantle from cluster analysis of long-period waveforms

C. Houser,*† G. Masters, P. Shearer and G. Laske

Institute of Geophysics and Planetary Physics, University of California San Diego, La Jolla, CA 92093, *USA. E-mail: creif@pmc.ucsc.edu*

Accepted 2008 February 15. Received 2008 February 15; in original form 2007 December 18

SUMMARY

We present a new technique for the efficient measurement of the traveltimes of long period body wave phases. The technique is based on the fact that all arrivals of a particular seismic phase are remarkably similar in shape for a single event. This allows the application of cross-correlation techniques that are usually used in a regional context to measure precise global differential times. The analysis is enhanced by the inclusion of a clustering algorithm that automatically clusters waveforms by their degree of similarity. This allows the algorithm to discriminate against unusual or distorted waveforms and makes for an extremely efficient measurement technique.

This technique can be applied to any seismic phase that is observed over a reasonably large distance range. Here, we present the results of applying the algorithm to the long-period channels of all data archived at the IRIS DMC from 1976 to 2005 for the seismic phases *S* and *P* (from 23° to 100°) and *SS* and *PP* (from 50° to 170°). The resulting large data sets are inverted along with existing surface wave and updated differential traveltime measurements for new mantle models of *S* and *P* velocity. The resolution of the new model is enhanced, particularly, in the mid-mantle where *SS* and *PP* turn. We find that slow anomalies in the central Pacific and Africa extend from the core–mantle boundary to the upper mantle, but their direct connection to surface hotspots is beyond our resolution. Furthermore, we find that fast anomalies that are likely associated with subducting slabs disappear between 1700 and 2500 km, and thus are not continuous features from the upper to lower mantle despite our extensive coverage and high resolution of the mid-mantle.

Key words: Mantle processes; Body waves; Seismic tomography.

1 INTRODUCTION

To date, seismic tomography has shed light on some of the most fundamental problems in geosciences (e.g. Dziewonski *et al.* 1977; Grand 1994; Su & Dziewonski 1997; van der Hilst *et al.* 1997; Masters *et al.* 2000; Megnin & Romanowicz 2000; Karason & van der Hilst 2001); see Romanowicz (2003) for a review. For example, there is now general agreement that slabs penetrate into the lower mantle but that there are clearly places where slab penetration is impeded. Thus, slab penetration into the lower mantle is not a steady-state process (e.g. Fukao *et al.* 2001). Tomography has also imaged large slow structures in the deep mantle that have characteristics that are not easily reconciled with simple thermal anomalies (Robertson & Woodhouse 1995, 1996; van der Hilst & Karason 1999; Masters *et al.* 2000; Saltzer *et al.* 2001; Beghein *et al.* 2002; Ishii & Tromp 2004). As resolution improves, finer-scale structure within these slow features becomes apparent and we can start asking interesting geodynamic questions, for example, are these features 'superplumes' or clusters of more 'normal' plumes (Schubert *et al.* 2004).

Resolution of tomographic models can be improved in several ways. Eventually, we may have the computing power to model the Earth using the entire seismogram (Komatitsch *et al.* 2002), but in the mean time, advances are being made in tomographic theory and data coverage. Recent developments in theory by Montelli *et al.* (2004a,b) have improved the recovery of slow anomalies in the mantle from traveltimes of seismic phases. Substantial improvements to seismic tomography, such as those presented here, also come in the form of better data coverage, either by taking advantage of the ever-expanding network of digital stations or by increasing the variety of seismic phases used in tomographic inversions.

This paper presents a new technique that combines cross-correlation with a cluster analysis method to efficiently construct large data sets of long-period traveltimes. Unlike short-period seismograms, in which the onset of a phase is often sharply and

*Now at: Department of Earth and Planetary Sciences, University of California Santa Cruz, Santa Cruz, CA 95064, USA.
†Formerly: Christine Reif.

unambiguously defined, long-period data have broad pulse shapes making it difficult to consistently determine the onset of a phase. Therefore, long-period phases need to be compared with similar long-period phases to measure their relative time-shifts (Woodward & Masters 1991a,b; Grand 1994; Bolton 1996; Ritsema & van Heijst 2002). Bolton (1996) and Bolton & Masters (2001) manually cross-correlated synthetic *P* and *S* pulses with the observed traces to record their arrival times. This method allows the researcher to visually inspect every trace that enters the traveltime catalogue and assign errors based on the confidence of the alignment of the synthetic and observed phases. However, the quantity of data now recorded means that manual trace-by-trace techniques of phase picking are far too time consuming. This has led Ritsema & van Heijst (2002) to develop a fully automated method for analysing long-period seismograms. As a result, they have to apply stringent quality control criteria to minimize the influence of noise or nearby phases on the measured time-shifts, significantly reducing the volume of data. Our new technique has minimal operator involvement and is based on the fact that all long-period arrivals of a particular seismic phase are often remarkably similar in shape for a single event. This allows the application of cross-correlation techniques that are usually used in a regional context to measure precise global differential times. The algorithm is enhanced by the inclusion of a clustering algorithm that automatically clusters waveforms by their degree of similarity. This allows the algorithm to automatically discriminate against unusual or distorted waveforms and makes for an extremely efficient measurement technique.

2 APPLICATION OF CLUSTER ANALYSIS

It has long been known that waveform cross-correlation can be used to produce more accurate differential times than can be obtained from individual arrival time picks (VanDecar & Crosson 1990; Rost & Thomas 2002). At long periods (> approximately 15 s), we have found that *P* or *S* waveforms from the same event can usually be correlated among global seismic stations (Reif *et al.* 2002; Rowe *et al.* 2002; Sigloch & Nolet 2006). Our method works as follows. First we pre-filter the data to the desired frequency band, separate the vertical and transverse components, crudely align the traces using the theoretical arrival time of the desired phase and display the results on the computer screen. The user then picks a time window for the cross-correlation. We compute cross-correlation functions for every trace with every other trace using a time domain method that achieves subsample accuracy. We identify the peaks in the cross-correlation function (both positive and negative) that contain the differential time and scaling information between the traces. Using cluster analysis (e.g. Hartigan 1975), the stations are sorted by the similarity of their waveforms and a cluster tree is plotted that shows at what level of correlation the various groups may be joined. The user then selects a minimum correlation coefficient to use as a cut-off for the cluster divisions. There is a trade-off between having a large number of clusters with highly similar waveforms and a smaller number of clusters with less-correlated waveforms. Optimal time-shifts for the stations within each cluster are then obtained using a L1-norm method, which also returns error estimates based on the internal consistency of the time-shifts. These values are typically very small as the cross-correlation functions are usually well defined.

We illustrate the technique with an earthquake in Kamchatka occurring in 2003 at a depth of 174 km. Fig. 1 shows all the transverse

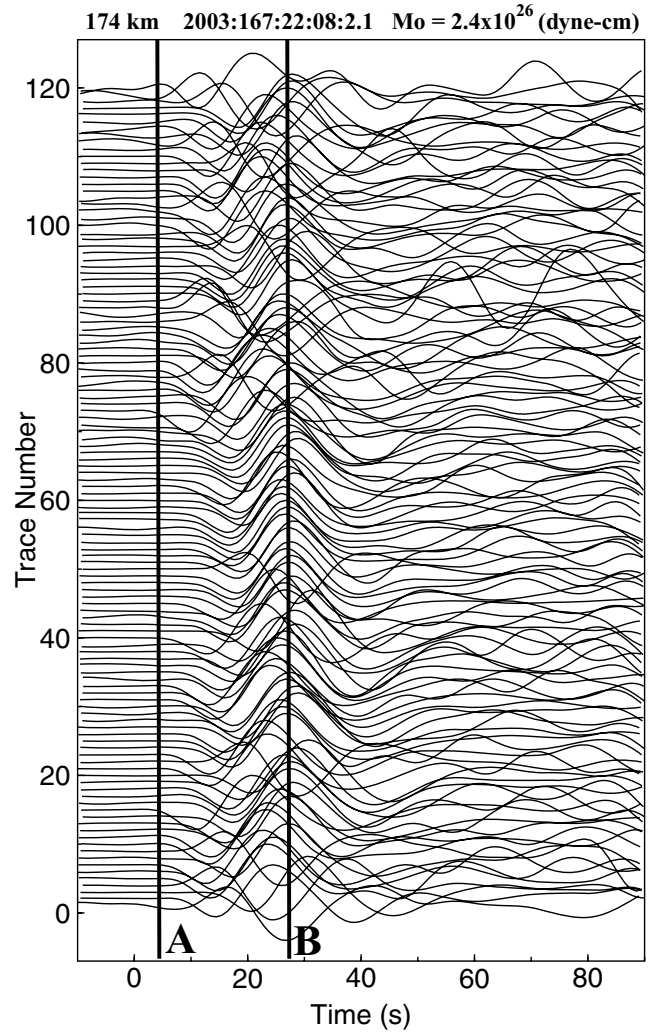

Figure 1. *S*-wave traces (transverse component) from globally distributed seismic stations aligned on their predicted PREM arrival time. Lines A and B represent the user-defined initial cross-correlation window used to align traces for further analysis shown in Fig. 2.

component traces for the earthquake that satisfy a specified signal-to-noise criterion for the *S* phase. We typically use only traces with a minimum signal-to-noise amplitude ratio of 4, since traces with smaller signal-to-noise ratios disrupt the correlation. We set a minimum threshold that each cluster must contain at least five traces that are initially aligned on the arrival time predicted by PREM (Dziewonski & Anderson 1981). The user-defined window for the cross-correlation is represented by the lines A and B in Fig. 1 and the correlations are performed to a time resolution of 1/8 of a second. The cross-correlation window is focused on the first swing of the pulse. Even though there is no tapering applied to the window function, the resulting cross-correlation functions are very stable. Fig. 2(a) shows the aligned traces based on the calculated best-fit time-shifts. The relative polarities of the traces are determined by the cross-correlation, and all traces are displayed with the same polarity. The 'distance and amalgamation' clustering algorithm described in Hartigan (1975) is applied using the correlation coefficients as a measure of 'distance' between traces. Pairs of highly correlated traces are identified by their correlation coefficients, averaged or 'amalgamated' together and treated as a single entity. This pairing

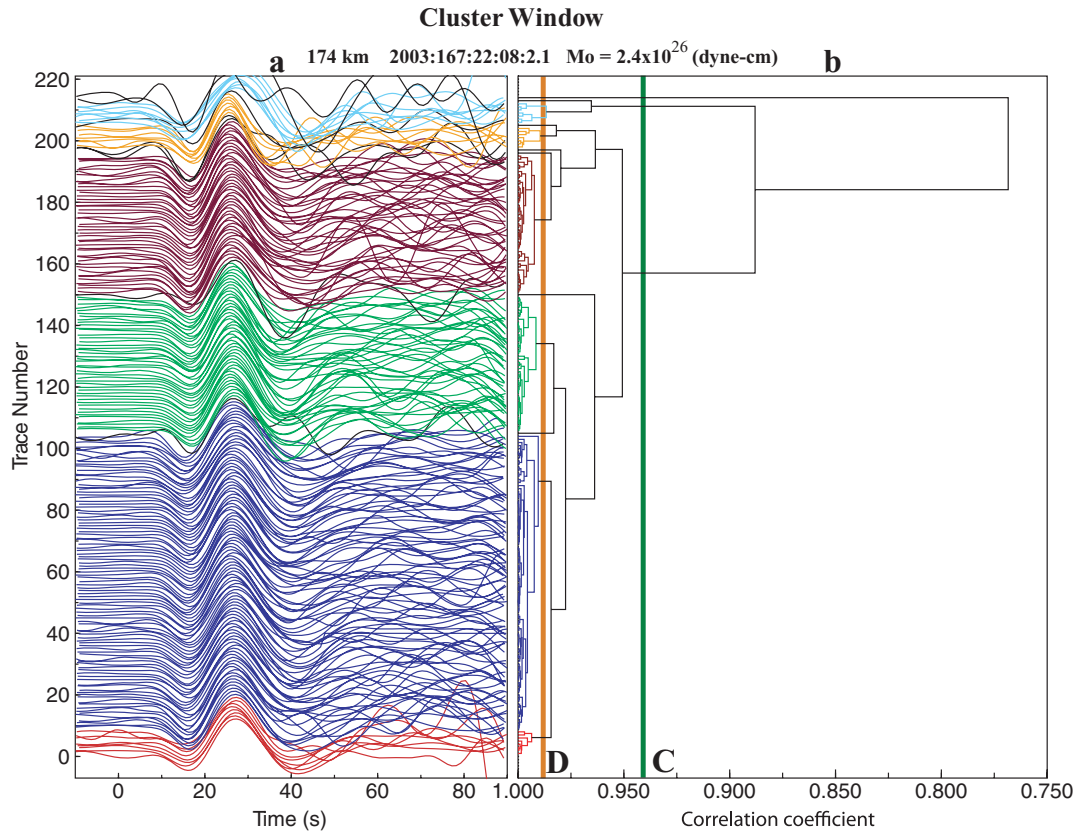

Figure 2. In the first panel (a) are the traces from Fig. 1 aligned on the cross-correlation determined time-shifts. The traces are colour-coded based on their grouping in the cluster tree in the second panel (b) and have been flipped to plot all with the same polarity. The second panel (b) is the cluster tree of the cross-correlation coefficients. Clusters are defined as any horizontal line lying to the left-hand side of and connected to the thin vertical lines. The dark green line C represents a cut-off that would combine the orange, maroon, green, dark blue and red traces into one cluster. The orange line D represents a cut-off that would separate the orange, maroon, green, dark blue and red traces into separate clusters. The light blue and black traces are not as highly correlated and would not be analysed further in the cluster analysis method.

and amalgamating process continues until every station is linked to at least one other station. As seen in Fig. 2(b), horizontal lines extend from each of the traces and are connected by vertical lines at each pairing level. Each vertical line defines a cluster, and the resulting cluster tree graphically represents how well correlated the traces are to each other. The traces in Fig. 2(a) are colour coded by their grouping on the cluster tree. The user determines at what level to separate the clusters for further analysis. For instance, the top traces (light blue and black) in Fig. 2(a) do not match well with the other traces, so a correlation level to the left-hand side of the vertical line that connects them with the other traces (represented by the vertical green line C in Fig. 2b) should be chosen. However, if the user thinks that the orange, green, dark blue and red traces should be in separate clusters, the orange line D should be chosen. Fig. 3 shows the geographic distribution of the stations for this event, colour-coded based on their clustering in Fig. 2. The dark blue and maroon clusters have global distributions while the orange, green and red clusters are more localized to certain regions. Fig. 4 demonstrates that both regionally and globally distributed clusters result from the clustering of long-period seismograms from a single event.

Once the level of clustering has been selected, such as line D in Fig. 2(b), the best-fitting time-shifts are re-calculated for each cluster. Fig. 4(a) shows only the traces of the dark blue cluster. Lines E and F represent the new user-determined cross-correlation window. The window is centred on the start of the pulse, since we wish to measure the relative arrival times of the pulses. Fig. 4(b) is the resulting window of the traces aligned according to the cross-correlation and flipped if necessary to have the same polarity. If the alignment is satisfactory, the median of the relative time-shifts is set to zero and the relative time-shifts and their associated errors are written to a file. It takes approximately 20 s to complete the process for each event. Starting in the late 1990s there are often more than 100 traces per event that satisfy the signal-to-noise ratio criteria, allowing us to accumulate very large data sets rapidly. The clustering also automatically isolates noisy or distorted records into separate clusters so it is not necessary to pre-screen the data for bad records.

Although it is possible to use the relative arrival times directly in an inversion for 3-D structure, we have found it beneficial to convert the data to absolute times. The knowledge of the absolute time allows us to identify clusters with large systematic time offsets, for example, if the direct phase is nodal and a later depth phase is misidentified as the direct phase. Since we have calculated the relative times among traces in a cluster, it is possible to get absolute times for the entire cluster by determining the absolute time of one trace. We take advantage of the similarity of the traces to combine them into an average trace to improve the signal-to-noise ratio. All the traces in the cluster are aligned according to their shift times, weighted according to their signal-to-noise ratios and summed to form the average trace. The absolute arrival time of the average trace is quickly determined by manually cross-correlating it with a synthetic trace calculated by normal mode summation. This

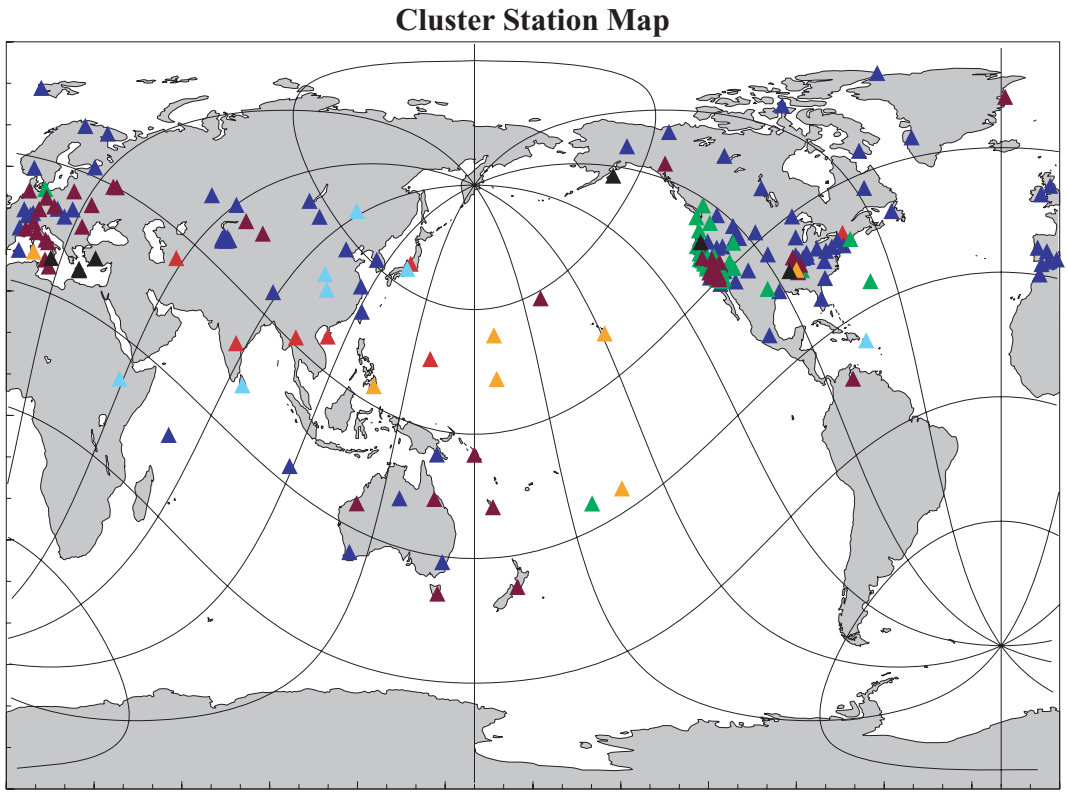

Figure 3. Global distribution of the seismic stations whose traces are displayed in Figs 1, 2 and 4. The stations are colour-coded based on their clustering defined by the orange line D in Fig. 2(b). Note the global distribution of stations in the dark blue and maroon clusters as opposed to the more regional distribution of the orange, green and red clusters. The pole of the projection is the earthquake location in Kamchatka.

absolute time is then added to the rest of the traces in the cluster to achieve absolute arrival times for the entire cluster. It is these absolute times that comprise the body wave data set used in our tomographic inversions. The errors on the cross-correlation are very small and not representative of the errors in measuring absolute traveltimes; thus, additional analysis is required to estimate the errors for the tomographic inversions and is discussed in detail in the next section.

This technique can be applied to any seismic phase that arrives over a long-enough distance interval such that there are enough high signal-to-noise traces per event to produce high quality clusters. In this paper, we have considered both direct *S* and *P* and *SS* and *PP*. An example of an *SS* and *PP* cluster for the same event is shown in Fig. 5. The highly emergent nature and greater variability of *SS* and *PP* arrivals increases the likelihood for cycle skipping and has led us to modify the cluster analysis slightly. *SS* and *PP* phases sometimes have an initial small amplitude up- or down-swing ahead of the main pulse, which can be observed in Fig. 5. This initial pulse can be misidentified as the main pulse in the cluster analysis method. We have found it more reliable to include a synthetic trace in the last stage of the clustering algorithm where the relative arrival times within a cluster are measured. The initial pulse in the synthetic trace provides a reference for aligning the initial pulses of the observed traces so that they are not confused with the main pulse.

We have applied the cluster technique to recordings from events with $m_b > 5.5$ from all global networks and available PASSCAL deployments for the years 1976–2005. *P* measurements are made from the vertical component recordings and *S* measurements from the transverse component. The records are deconvolved to remove the initial station response and then filtered to the old SRO station response so that all the traces have the same frequency content. The resulting seismograms have a dominant period of about 25 s. We exclude body waves that turn above 700 km depth as their waveforms are distorted by the transition zone discontinuity triplications. *SS* and *PP* measurements are made in the distance range from 50° to beyond 180° though only 3 per cent of the data extend beyond 160° in our *SS* and *PP* data catalogue. This is a result of the decreased probability of measuring arrivals at these distances as well as the increased complexity of the waveforms because of interference near the antipode. Histograms of the *S*, *SS*, *P* and *PP* demeaned absolute traveltime residuals are shown in Fig. 6. The residuals are initially defined as the observed arrival time minus that predicted by the normal mode summation using AK135 (Kennett *et al.* 1995), however when demeaned, they become independent of the initial 1-D model. In addition, the absolute time residuals have been analysed to remove outliers following the procedures described by Bolton & Masters (2001) and corrected for station timing errors.

The time range and number of data for cluster analysis *S*, *SS*, *P* and *PP* as well as our hand-picked differential data sets are shown in Table 1. Our cluster analysis *S* and *P* data sets are substantially larger than those used to make SB4L18 (Masters *et al.* 2000), in which 41 000 *S* and 38 000 *P* arrival times were used in the inversion. We have also updated the *ScS*–*S* data set, more than doubling the number of measurements (8000) used to make SB4L18. The *SS*–*S* and *PP*–*P* data sets have been modestly updated from 18 000 and 12 000 measurements, respectively. In addition, we have obtained entirely new data sets of *SS* and *PP* phases. This new compilation of data is motivation for producing new tomographic models of shear and compressional velocity anomalies throughout the mantle. The improvement of data coverage compared with the data sets used to

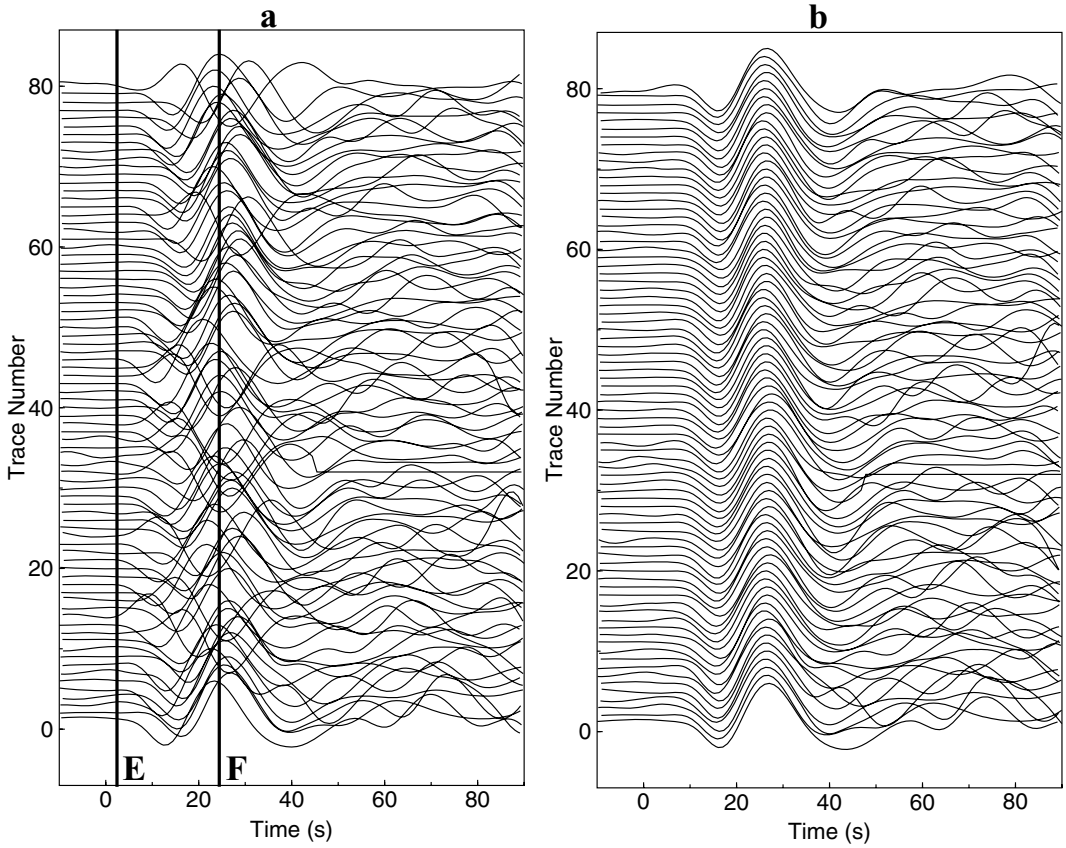

Figure 4. In the first panel (a) are the traces from the dark blue cluster from Fig. 2 aligned on their predicted PREM arrival time. Lines E and F represent the user-determined cross-correlation window. The second panel (b) shows the blue cluster alignment based on the cross-correlation window defined in the first panel (a).

build SB4L18 is shown in Fig. 7. To have the most complete set of long-period traveltimes possible, we combine the *S* and *P* times that contributed to the Masters *et al.* (2000) study that were not present in our cluster analysis derived traveltimes for the inversion of shear and compressional velocity structure of the Earth's mantle.

3 THE INVERSION

The traveltime residuals with respect to a 1-D Earth are dominated by two signals, source mislocation and 3-D structure. Application of the summary ray analysis of Bolton & Masters (2001) to separate the effects of mislocation and 3-D structure suggests that the source mislocation effects are around 0.6 s for *P* and 1.6 s for *S*. The effect of 3-D structure on the traveltimes is similar to that found by Bolton & Masters (2001), around 1.2 s for *P* and 3.5 s for *S*. Clearly, source mislocation accounts for about a third of the total signal and so must be accounted for properly in the inversion.

The mislocation effects are removed using a projection operator, **P** (Masters *et al.* 1996). The algebraic system describing the traveltime residuals, δt, can be expressed as

$$\delta t = \mathbf{B} \cdot h + \mathbf{A} \cdot \frac{\delta v}{v}, \tag{1}$$

where **B** is a matrix containing the source–receiver geometry, h is a four-vector describing a perturbation in location and origin time of the event, **A** is the matrix of ray path lengths (scaled by the 1-D velocity model) in each block of the model and $\delta v/v$ is a vector of velocity perturbations describing 3-D velocity structure. A projection matrix **P** is calculated such that $\mathbf{P} \cdot \mathbf{B}$ is zero.

$$\mathbf{P} \cdot \delta t_e = \mathbf{P} \cdot \mathbf{A} \times \frac{\delta v}{v}. \tag{2}$$

Each row of eq. (1) is typically divided by the observational error so that the covariance matrix of the data is just the identity matrix. **P** is chosen such that the resulting covariance matrix of the projected data $\mathbf{P} \times \delta t_e$ is diagonal so that the new data are independent, where δt_e indicates the error-weighted traveltime residuals. The very small error values that result from the cluster analysis reflect the internal consistency of the clustering algorithm rather than traveltime errors associated with Earth structure. Therefore, we use the errors associated with 3-D structure in the summary ray analysis for the inversion. These values range from 0.7 to 2.4 s for *S*, 1.4 to 2.5 s for *SS–S*, 0.85 to 1.5 s for *ScS–S* and a constant value of 2.5 s for *SS* as well as 0.5 to 1.6 s for *P* and *PP–P* and a constant value of 2.1 s for *PP*, depending on the quality of the average trace used to determine the absolute arrival time of the cluster. The projection matrix takes a linear combination of the data, which, to first order, are insensitive to location. Since we also require that the new projected data be independent, we lose four data per event.

We use a block model parametrization for the mantle with 18 layers of equal-area blocks having 4° width at the equator, resulting in 46 404 model parameters. The blocks in the upper mantle have approximately 100 km thickness and blocks in the lower mantle have thickness of approximately 200 km. The blocks are thinner in the upper mantle to fit the surface wave data, which require large velocity

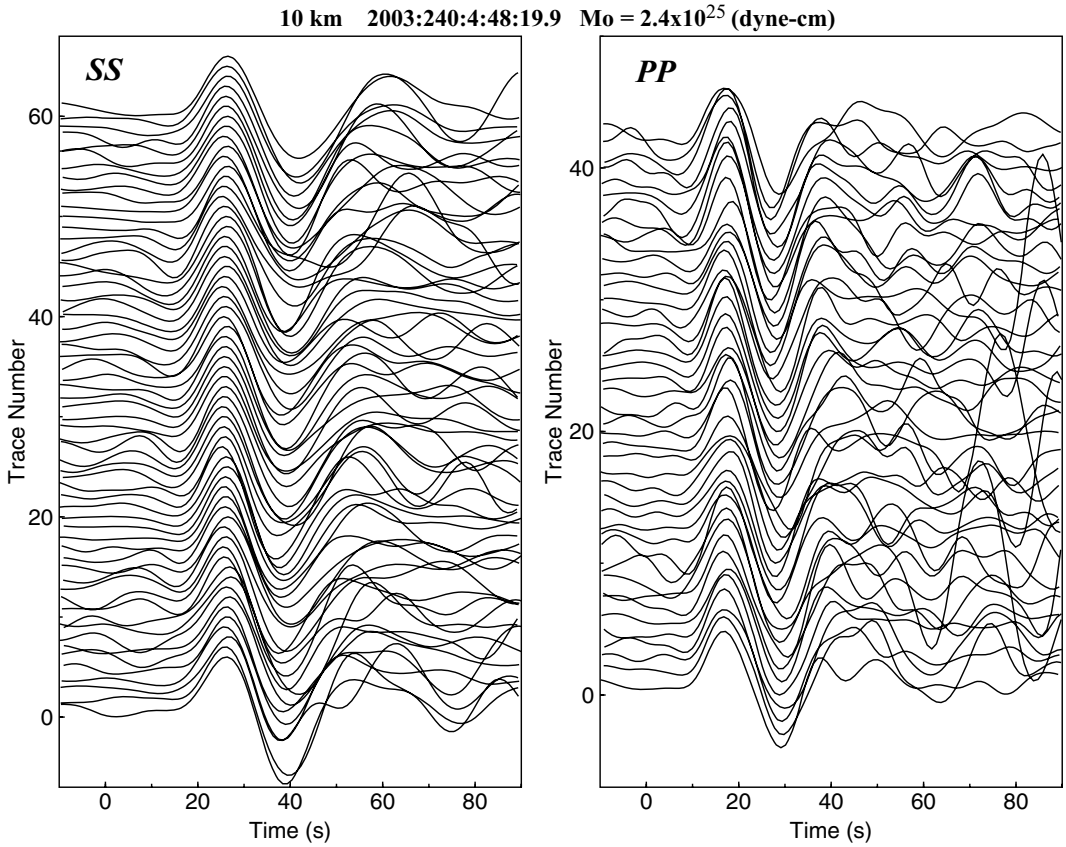

Figure 5. *SS* (left-hand side) and *PP* (right-hand side) clusters after alignment.

gradients in the uppermost mantle. The ray paths are calculated through the 1-D model, AK135 (Kennett *et al.* 1995).

Body wave data are most sensitive to structure at their turning point. To avoid complications in the waveforms due to the triplications in the mantle transition zone, we only use waves turning in the lower mantle. The data set, therefore, loses sensitivity to upper-mantle structure because all the ray paths are nearly vertical there. To constrain the shear velocity model in the upper mantle, we use the surface wave phase velocity maps of Love (Bassin *et al.* 2000) and Rayleigh (Laske 2004, personal communication) waves at frequencies of 4–15 mHz, listed in Table 1. The lateral coverage of these data sets is excellent and the lowest frequencies are capable of constraining structure in the transition zone. Finally, we also include handpicked differential *PP–P*, *SS–S* and *ScS–S* data collected using the methods of Woodward & Masters (1991a,b). The effects of crustal thickness variations are removed using CRUST 2.0 (Laske *et al*., http://mahi.ucsd.edu/Gabi/rem.dir/crust/crust2.html).

We use the LSQR method (Paige & Saunders 1973) to iteratively invert for the velocity perturbations using the following system of equations:

$$\frac{\delta v}{v} = \begin{bmatrix} \mathbf{P}\cdot\mathbf{A} \\ \lambda_1\mathbf{D}_R \\ \lambda_2\mathbf{D}_L \end{bmatrix}^{-1} \times \begin{bmatrix} \mathbf{P}\cdot\delta t_e \\ 0 \\ 0 \end{bmatrix}, \tag{3}$$

where to have a well-conditioned matrix for the inversion, radial (λ_1) and lateral (λ_2) smoothing parameters are applied to radial, $\mathbf{D}_R$, and lateral, $\mathbf{D}_L$, first difference operators. Although we have more data than model parameters, some smoothing is necessary, since the ray geometry leaves some areas of the model poorly constrained. The parameters λ_1 and λ_2 are chosen such that further roughening of the model does not provide a significant improvement in the fit to the data. Choosing the proper smoothing parameters is a subjective process, but our goal is to maximize the resolution of small-wavelength features without increasing the uncertainty in our models. In addition, the inversion is optimized such that the χ^2/N fit of the model to the combined projected data is close to 1. The χ^2/N values for the individual shear phases are 6.2, 3.5, 3.6 and 1.77 for *S*, *SS*, *SS–S* and *ScS–S*, respectively, and for the compressional phases we find 3.5, 1.3 and 1.5 for *P*, *PP* and *PP–P*, respectively. These values are all greater than one due the influence of mislocation on the time residuals that is mostly removed by the projection procedure. The large volume and variety of the cluster analysis data sets allow us to lower the smoothing parameters from what had been appropriate for the previous modelling of Masters *et al.* (2000). Thus, the shear velocity model presented here has greater detail in the structure of anomalies and better recovery of amplitudes than previous long-period studies, especially in the mid-mantle where our coverage is most complete.

4 SHEAR VELOCITY MODEL RESULTS

Our new shear velocity model (Figs 8 and 9) reveals similar structures to recent models built using long-period traveltimes (Masters *et al.* 2000; Antolik *et al.* 2003; Simmons *et al.* 2006). Fig. 8 shows depth slices of our shear velocity model, HMSL-***S***06, throughout the mantle. The blue regions are faster than the average mantle at that depth and likewise the red regions are slower. The white regions indicate that the anomaly is below the average error of the model,

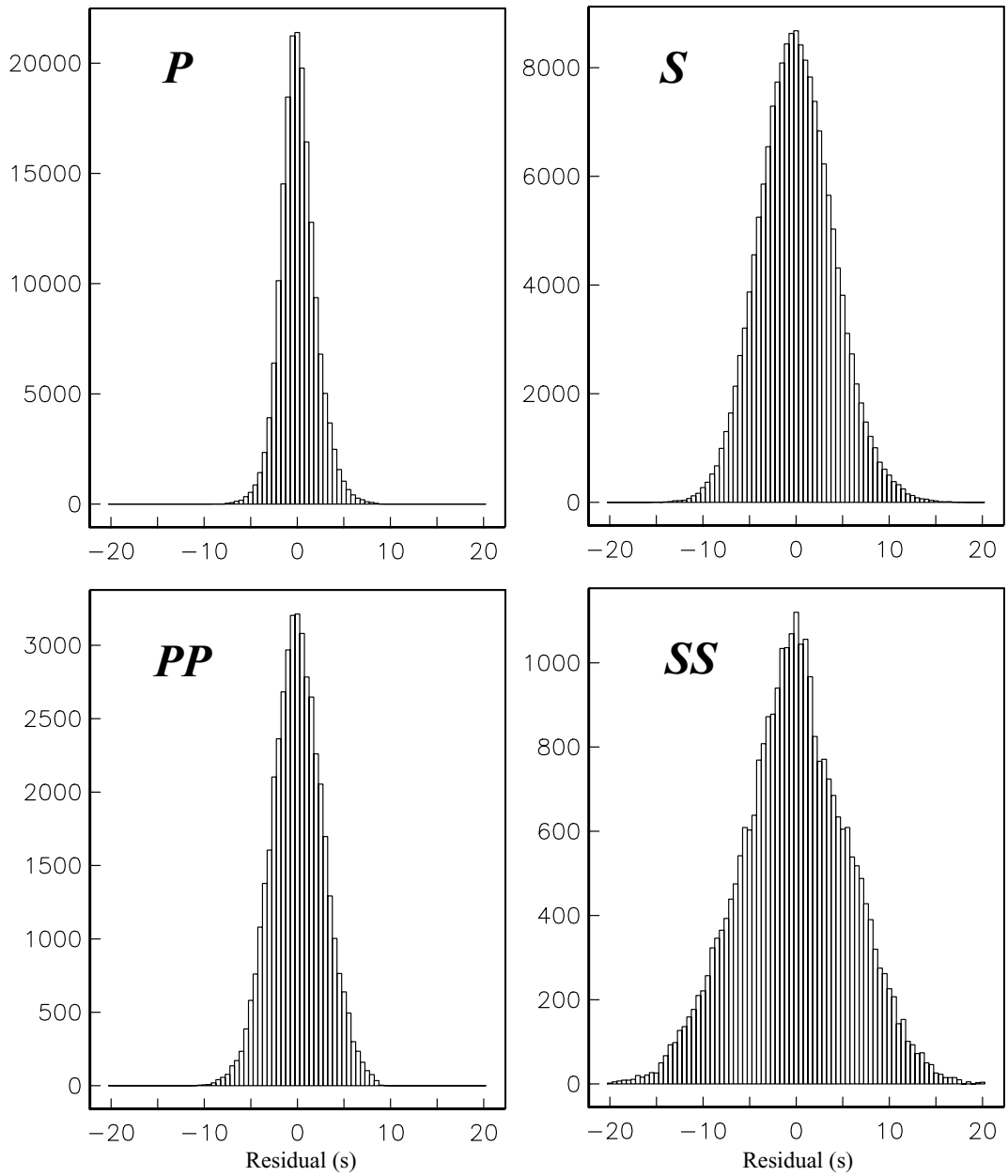

Figure 6. Histograms of the cluster analysis *P*, *S*, *PP* and *SS* demeaned time residuals.

Table 1. Data sets.

Data type	Start	End	Number of data
S	1976	2005	169 832
P	1976	2005	182 724
SS	1995	2005	28 194
PP	1995	2005	42 710
SS–S	1976	1999	27 560
PP–P	1976	1999	22 595
ScS–S	1976	2005	26 840
Love waves	1989	1999	14 000
Rayleigh waves	1989	1999	42 000

about 10 per cent of the largest anomaly, as determined from the Monte Carlo error analysis described below. For most of the mantle, the anomalies range in ±2 per cent, however the range can exceed ±4 per cent in the uppermost and lowermost mantle.

Notable features in the shear velocity model are the broad regions of slow and fast anomalies in the lowermost mantle, the lack of fast slab-like features in the lower portion of the mantle (1700–2500 km), vertical slow plume-like features under the Pacific and African plates and the appearance of slab ponding in the transition zone. These features are best demonstrated in Fig. 9, which shows isovelocity contours where blue is +1 per cent fast and red is −1 per cent slow in a 3-D spherical mantle. The slow anomalies at the core–mantle boundary (CMB) under the Pacific and Africa, often referred to as 'superplumes', are clearly visible. The only vertically coherent features from the lower to upper mantle are the narrow slow features under the central Pacific and African plates. Their locations suggest they may be related to the Hawaii, Canary Islands or Afar hotspots. Before discussing the features of the model further, it is necessary to reveal the strengths and weaknesses of our model's ability to recover structures in the mantle.

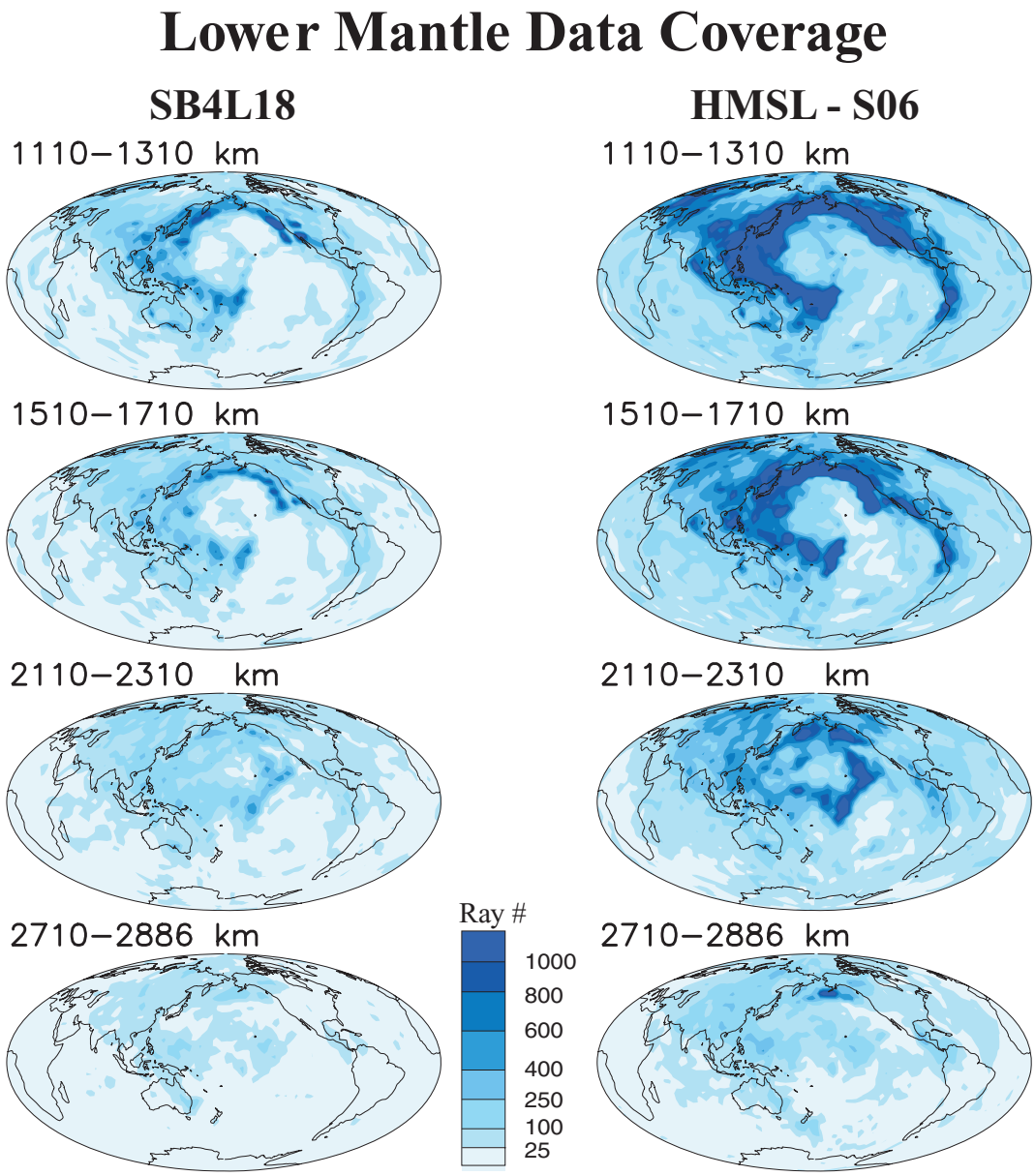

Figure 7. Maps of the body-wave data coverage for the data sets used to build SB4L18 (right-hand side) and the shear velocity model presented here, HMSL-***S***06 (left-hand side). The scale is based on the number of times a model block is traversed by the *S*, *SS*–*S*, *ScS*–*S* and, in this study, *SS* ray paths.

Checkerboard tests provide a visual evaluation of the resolution of tomographic models. A checkerboard test consists of calculating synthetic data using eq. (2) for a known model and then inverting the synthetic data to compare the output model with the input model. Fig. 10(a) is a checkerboard test model for a single layer used to produce the synthetic data. The inversion of the synthetic data allows us to determine the ability of our ray path geometry to resolve the input checkerboard pattern, taking into account the smoothing parameters used in the actual inversion. The initial checkerboard is constructed using a spherical harmonic pattern of degree $l = 15$ and $m = 7$ which corresponds to blocks of about 12°. Figs 10(b)–(d) show the recovered shear velocity model above, at and below the 530–660 km input layer. Likewise, Figs 10(e)–(g) show the recovery for a checkerboard in the 1710–1910 km layer, and Figs 10(h) and (i) in the layer above the CMB. Checkerboard tests reveal the ability of the data to recover both the pattern and the amplitude of the input checkerboard. In the transition zone, there is relatively poor depth control of the long-period fundamental mode surface waves used in this study. The result is that the lateral resolution is good due to the global coverage of surface waves, but only regions well sampled by the body waves recover the amplitude of the original checkerboard model, mainly in the circum Pacific area. In the mid- and lower-mantle, the body wave data provide both good lateral resolution and good amplitude recovery. However, this lateral recovery breaks down in the Southern Hemisphere near the CMB. Even in poorly resolved regions of the lower mantle, there is almost no radial smearing. To summarize, structures in the transition zone are well-resolved laterally, but may be smeared in depth. Structures in the mid- and lower-mantle are well resolved both laterally and radially, and structures near the CMB are well resolved in the

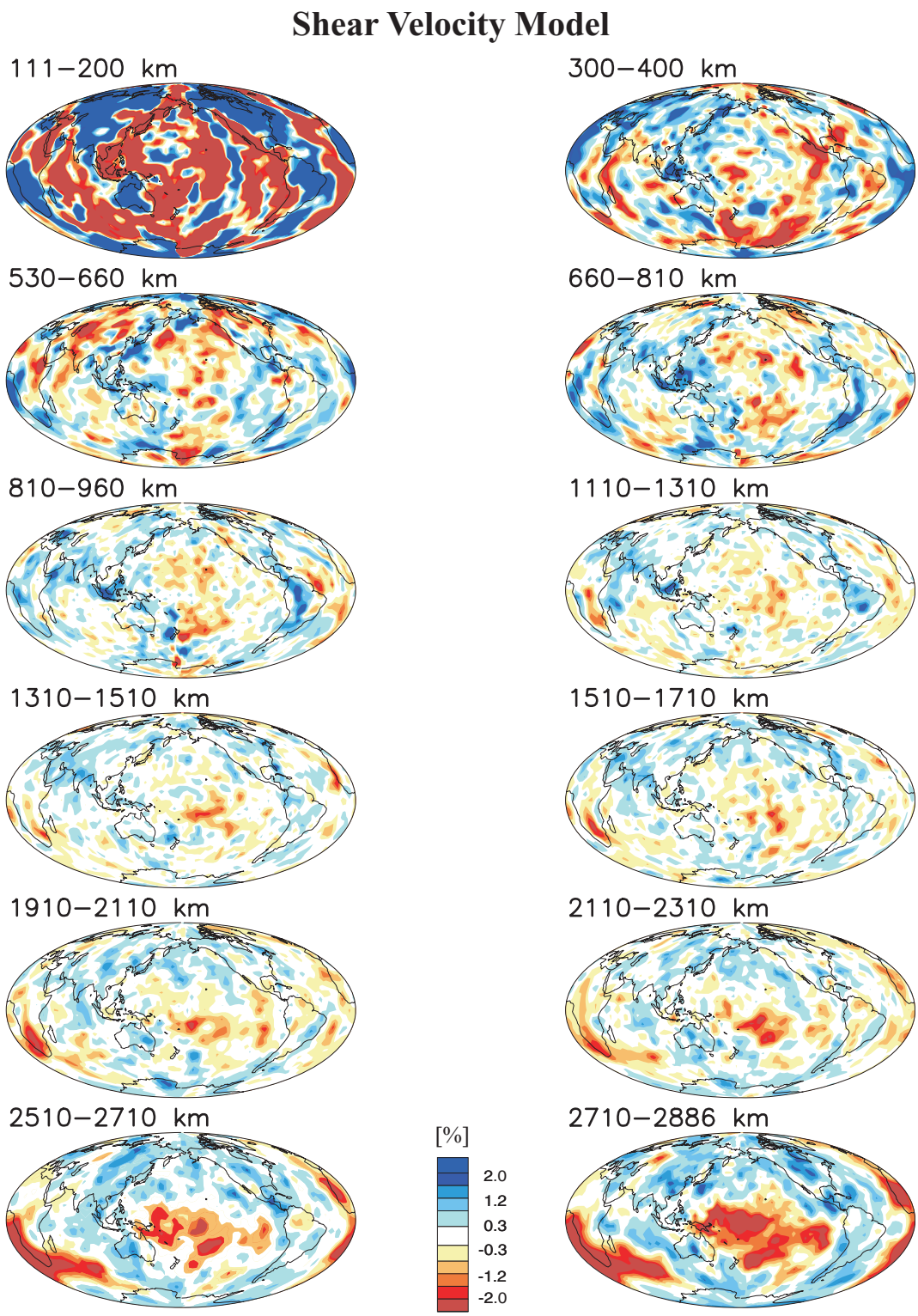

Figure 8. Depth slices of our cluster analysis shear velocity model, HMSL-***S***06, where the mean from each layer has been removed. Dark red and blue areas represent anomalies that are 2 per cent slow and fast, respectively. The largest anomalies occur within a few hundred kilometres of the surface and the core–mantle boundary (CMB).

Northern Hemisphere, but the resolution decreases in the Southern Hemisphere.

In the upper mantle, slabs are too narrow to be resolved by long-period body wave or surface wave data. Fast anomalies associated with cold subducting slabs are found in the transition zone, indicating that slabs are accumulating or 'ponding' there. Fast anomalies present from 800 to 1700 km depth beneath North and South America and are believed to be remnants of the Farallon slab (Grand 1994)

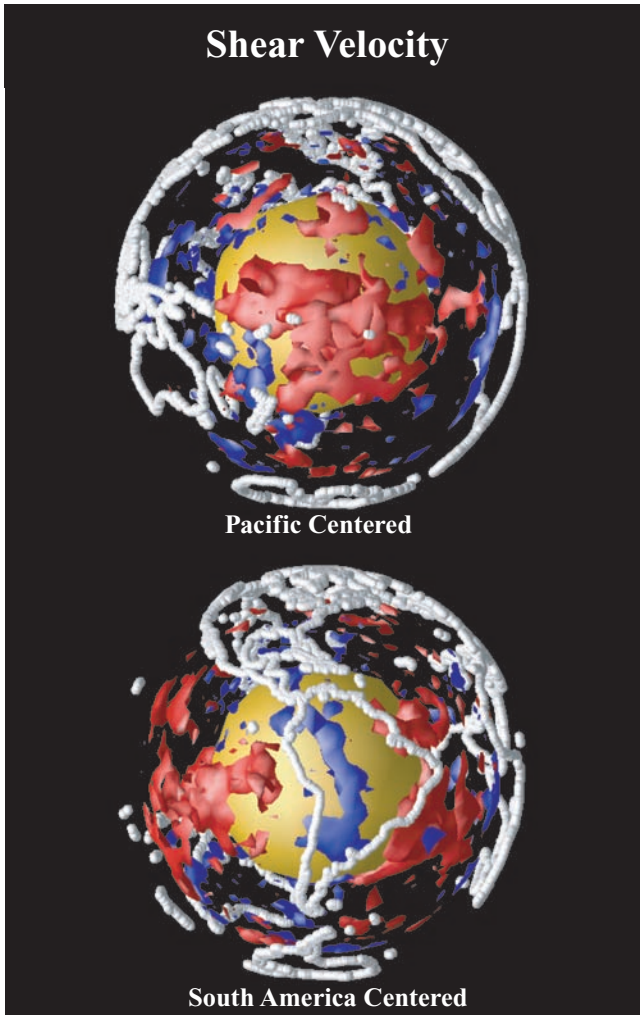

Figure 9. 3-D views of our shear velocity model. The Pacific centred view at the top best illuminates the circum Pacific fast anomalies, and the South America centred view on the bottom illuminates the Pacific and African slow anomalies. Blue isovelocity contours outline 1 per cent fast anomalies and red isovelocity contours outline 1 per cent slow anomalies. Anomalies in the top 300 km have been removed to allow viewing into the lower mantle.

and beneath the Mediterranean and northern India are believed to be remnants of the Tethys slab (van der Hilst & Karason 1999). The presence of these slab signatures suggests that slabs do pass through the transition zone into the lower mantle. The lack of vertically coherent fast anomalies below 1700 km implies that subducting slabs may be too distorted to produce a long-period seismic signature or that subduction is an intermittent process. The mid-mantle of our model is abundantly sampled by our body wave data (Fig. 10), therefore, any large-scale structure there would be resolved.

5 COMPRESSIONAL VELOCITY MODEL RESULTS

Creating a reliable compressional velocity model of the entire mantle from long-period body wave data is not a trivial task. Love waves are completely insensitive to compressional velocity, and Rayleigh waves have little sensitivity except close to the surface. The body waves used in this study travel essentially vertically in the upper mantle and thus are not able to localize velocity structure in the upper mantle. From the shear velocity model, we know that there are very large shear velocity anomalies in the uppermost mantle that are also likely to exist in compressional velocity. We therefore, account for upper-mantle structure by inverting the *P* data with a constraint matrix that scales the compressional model above 660 km to the shear velocity model:

$$\frac{\delta v_s}{v_s} = 1.7\frac{\delta v_p}{v_p}, \tag{4}$$

where 1.7 is the expected value if the anomalies are due to purely thermal effects (Karato 1993). In addition, an analysis of the *PP–P* and *SS–S* data suggests that *P* and *S* velocity are correlated according to eq. (4) (Woodward & Masters 1991b). Applying this scaling does not affect the fit of the compressional velocity model to the *P* data.

The final *P* velocity model, HMSL-***P***06, is shown in Figs 11 and 12 and correlates quite strongly with the shear velocity model (Figs 8 and 9). This is to be expected as *P* waves have high sensitivity to the shear modulus. However, the large amplitude structure at the base of the mantle appears to be significantly different. Fig. 13 shows the resolution capability of the *P* data. Arranged similarly to Fig. 10, Fig. 13 demonstrates the initial checkerboard (a) and its recovery for the 660–810 layer (b)–(d), the 1710–1910 layer (e)–(g) and the layer above the CMB (h) and (i). We show the 660–810 layer in Fig. 13 instead of the 530–660 layer as in Fig. 10 since the *P* model is constrained to the *S* velocity model in the transition zone. The *P*-velocity model recovery is very similar to that of the *S*-velocity model, except that there is decreased resolution in the Northern Hemisphere near the CMB. However, the resolution of both the *P*- and *S*-velocity models in the central Pacific at the CMB is robust enough to provide confidence that the differences in structure there are real.

There are actually over twice as many *P* rays that turn in the range of 2700–2886 km depth than *S* rays. Unfortunately, although these provide tight constraints at their turning points, the lateral coverage is not as good as that of *S*. Moreover, the addition of the *ScS–S* coverage does much to improve the lateral coverage for shear velocity near the CMB. The data coverage of the *P* and the combined *S* and *ScS* data sets are shown in Fig. 14. The *P* residuals, Fig. 14(a), and the combined *S* and *ScS–S* residuals, Fig. 14(b), are binned and averaged at their turning points. The binning caps are 4° in radius and only caps with more than three measurements are plotted. The scale of the *P* residuals is less than that for the *S* residuals. Visual inspection of the maps shows that the *P* and *S* residuals are correlated, which is shown quantitatively in Fig. 14(c), where the *P* and *S* residuals are plotted against each other for matching bins. The orange line has a slope of 3, which is the predicted relation between the two for thermal effects (Karato 1993) and fits the data for most of the mid- and lower-mantle. However, in the lowermost mantle, the data are actually better fit with a slope close to 6 (yellow line), which is in agreement with the results of Bolton & Masters (2001).

We expect the compressional model and the shear model to have similar structures in the lower mantle. As in the shear model, there are slow velocity anomalies beneath southwest Africa and the central Pacific in the compresssional model; however, with smaller magnitude and less extent than the shear model. There is little structure in the mid-mantle except for slow features that are vertically coherent from the central Pacific and African lower to upper mantle. This connection is apparent in the 3-D image of the compressional

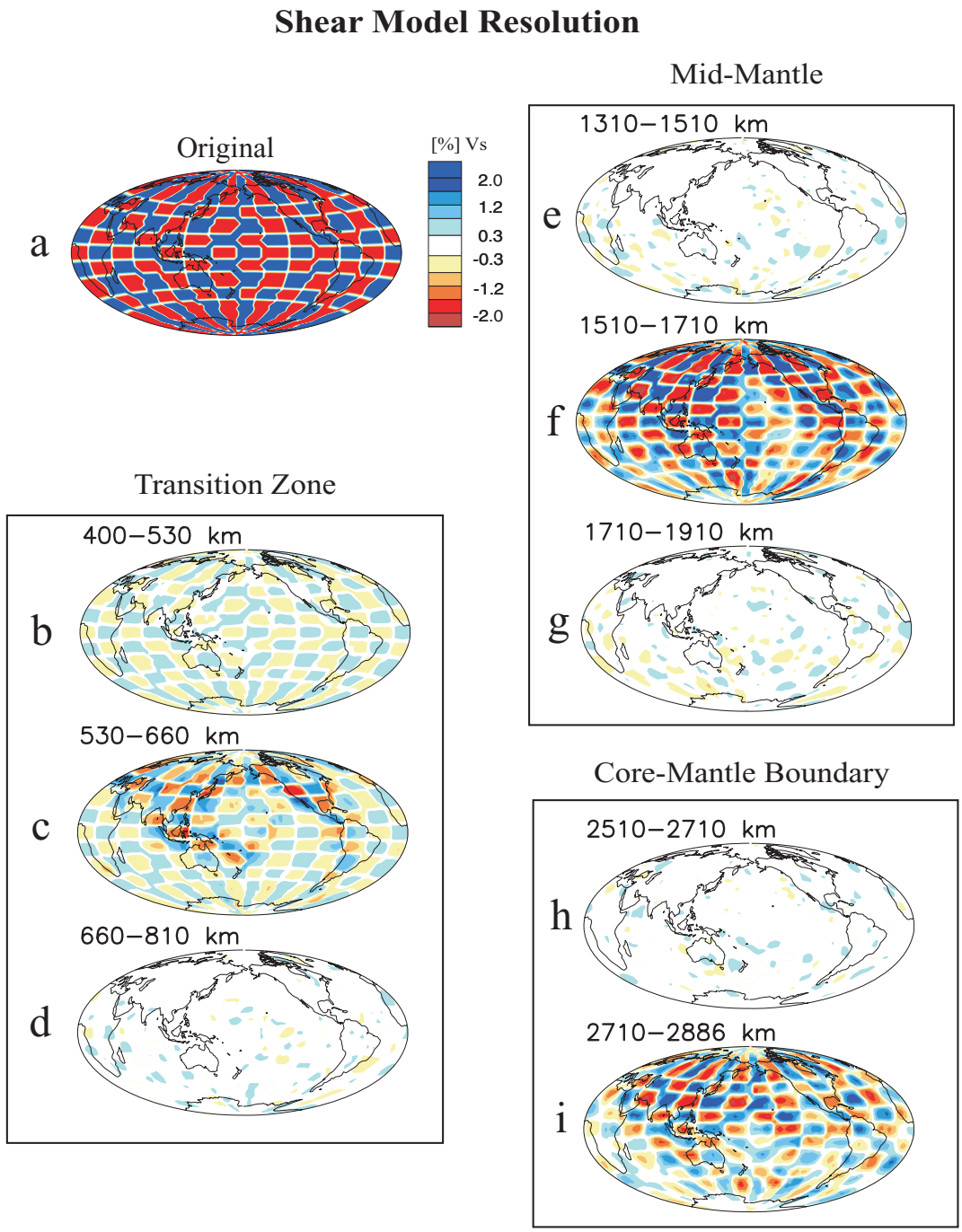

Figure 10. Checkerboard tests (a) applied to our shear wave data sets for an input layer in the transition zone (b–d), the mid-mantle (e–g) and the lowermost mantle (h and i). The checkerboard is best recovered in the mid-mantle. The same ray geometry and smoothing was used as in the case of the real data.

velocity model (Fig. 12) where the blue and red isovelocity contours are plotted at the ±0.6 per cent velocity anomaly level in a 3-D spherical mantle. The slow features have a somewhat different structure than in the shear model. The linear, fast anomalies associated with Farallon and Tethys slabs are very prominent down to 1500 km depth. In the lower mantle, the fast anomalies become more diffused and then re-appear in the circum Pacific of the lowermost mantle, with very fast regions under eastern Asia and Central America.

6 MODEL ERROR

To determine the stability of the structures in our model, we perform a Monte Carlo error analysis in which we add noise to the data and invert for a new model, repeating this process 100 times. The noise has a Gaussian distribution and standard deviation identical to that of the data. This procedure is different from boot strapping since we maintain the same ray geometry, but apply noise to the data to test the sensitivity of the model to slight variations in the data. If a region

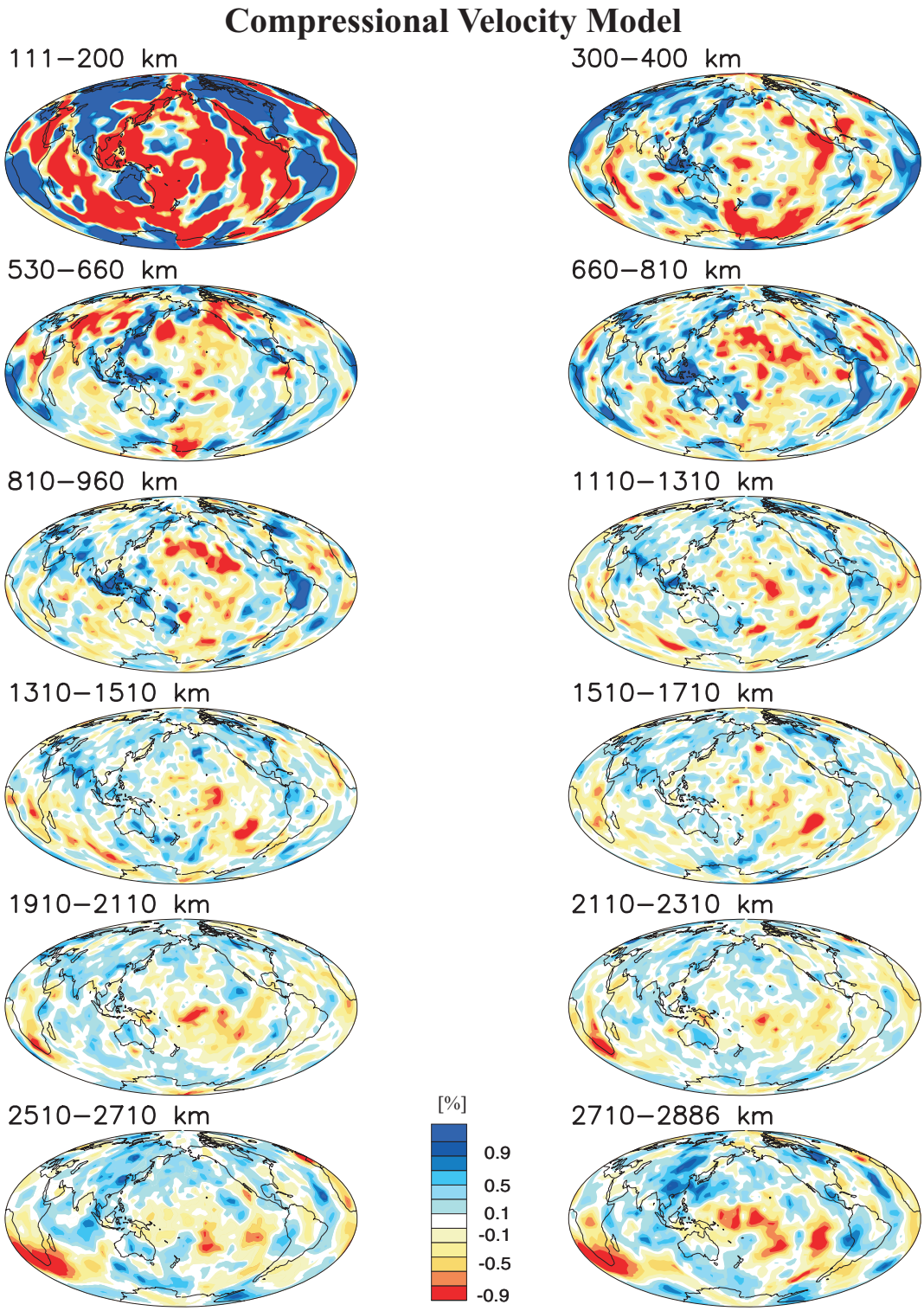

Figure 11. Depth slices of our compressional velocity model, HMSL-***P***06, using the cluster analysis body wave data. Dark red and blue areas represent anomalies that are 1 per cent slow and fast, respectively.

is well sampled, then the random noise will cancel and the structure will not vary from model to model. However, in regions that are not well sampled, noise in the data can translate into changes of structure in the models. The standard deviation of the models from our 100 inversion runs is our computed estimate of the error. The standard deviation is mapped in Fig. 15 for the *P* model (left-hand side) and the *S* model (right-hand side). The green areas represent well-constrained regions of the models. The upper mantle of the *P* model has a very low standard deviation due to the constraint that it be a scaled version of the *S* model in the upper mantle.

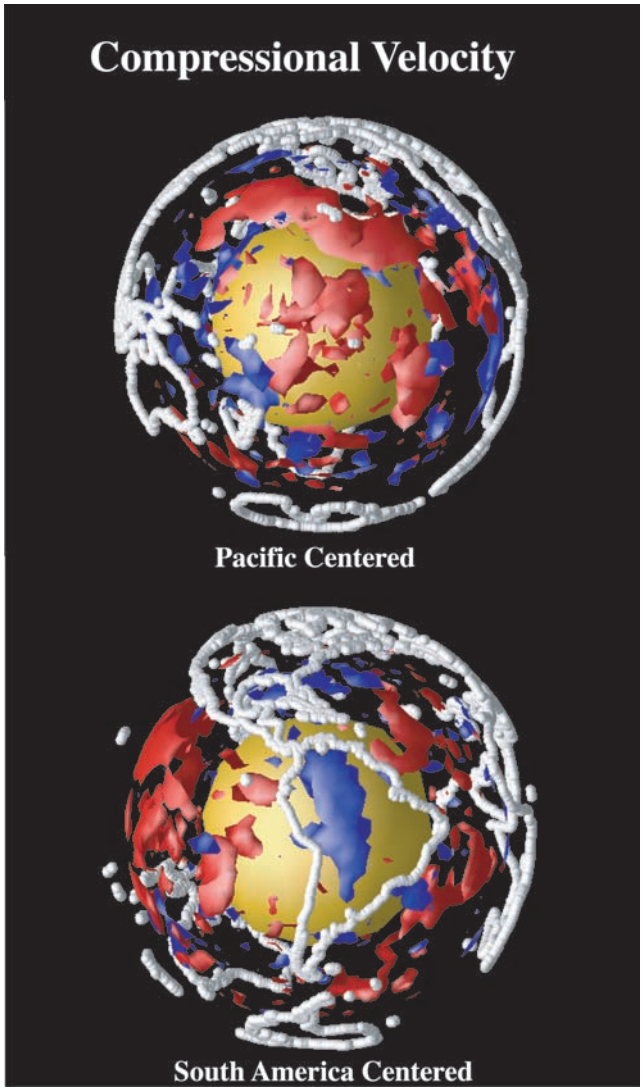

Figure 12. 3-D view of our compressional velocity model. The Pacific centred view at the top best illuminates the circum-Pacific fast anomalies, and the South America centred view on the bottom best illuminates the Pacific and African slow anomalies. Blue isovelocity contours outline 0.6 per cent fast anomalies and red isovelocity contours outline 0.6 per cent slow anomalies. Anomalies in the top 300 km have been removed to allow viewing into the lower mantle.

The Monte Carlo error analysis, along with the resolution analyses (Figs 10 and 13), indicates that, in both models, features in the Northern Hemisphere of the lower mantle and mid-mantle are robust. Fig. 15 reveals that the areas of larger error in our models are mainly the eastern Pacific in the mid-mantle and the Southern Hemisphere in the lowermost mantle. These areas of larger error result from the lack of coverage dictated by the source–receiver geometry. The error in the shear velocity model increases just above the transition zone because the sensitivity of the surface waves generally decreases with depth, although our longer period surface waves have some sensitivity into the transition zone. The resolution and error analyses indicate that we can recover the basic structure of the lower mantle, but have difficulty recovering the full amplitude of anomalies where coverage fades.

7 CONCLUSIONS

We have combined the speed of cross-correlation techniques with the quality control of clustering algorithms to develop a new long-period seismic data analysis technique, referred to as 'cluster analysis'. The cross-correlation rapidly computes the relative arrival times, and the clustering allows the user to visually inspect the entire data set and group the waveforms appropriately. The data are used to compute shear and compressional velocity models throughout the mantle.

Our velocity models reveal the fate of subducted oceanic lithosphere, or slabs, as they descend into the lower mantle. Dynamic models of subducting slabs have conflicting results. For example, Tan & Gurnis (2002) find that slabs should retain a continuous thermal anomaly to the CMB as opposed to the Machetel & Weber (1991) model in which slabs collect above the 660 km discontinuity before falling or 'avalanching' into the lower mantle. The long-period surface and body wave data used in this study are sensitive to structure with minimum wavelengths of about 250 km. Since slabs have thickness of about 100 km in the upper mantle, they are too thin to be detected by our data. However, fast anomalies do become apparent in the transition zone in both our shear and compressional velocity models. Therefore, the slabs must be collecting in the transition zone. This could be due to the endothermic phase transition at the 660 km discontinuity, an increase in viscosity in the lower mantle, bulk chemistry differences between the upper and lower mantle or a combination thereof. However, slabs are also imaged below the transition zone, indicating that they are not permanently confined there.

In both our shear and compressional velocity models, we interpret fast anomalies as slabs collecting in the transition zone under the Aleutian, Japan, Izu-Bonin, Philippine, Java and Marianas trenches in the northern and western Pacific. The Tonga and South American slabs are observed as weak fast anomalies in the transition zone, but are clearly defined between 660 and 1000 km. At around 850 km, fast anomalies emerge under North America and Eurasia, which are likely the remnants of the Farallon and Tethys slabs. These extend to about 1700 km depth. At 2500 km depth, fast anomalies appear in a ring around the Pacific. Although these fast anomalies are geographically coincident with past and current subduction zones, it is not certain whether or not they are directly related.

Due to the absence of slabs between 1700 and 2500 km, our models do not reveal a direct connection with the upper-mantle fast anomalies and those in the lowermost mantle. The lack of a slab signature in the lower portion of the mantle is not due to a lack of resolution, since our data sets are large and have good coverage throughout the region. There are several explanations for the absence of slabs. It is possible that the slabs are being deformed at scales smaller than our model parametrization (around 400 km) or are equilibrating with the mantle. Alternatively, subduction is not a continuous process since the slabs are often delayed in the transition zone. Therefore, it could be that the absence of fast anomalies in the lower mantle represents a time gap of slabs penetrating into the lower mantle. Our models are not able to distinguish between these hypotheses.

The fast anomalies at the CMB are thought to be the collection of slab material there (van der Hilst *et al.* 1997), although, to date, this interpretation is difficult to prove or disprove. Looking at the geological record of subduction and the geoid, Ricard *et al.* (1993) and Lithgow-Bertelloni & Richards (1998) found slabs at the

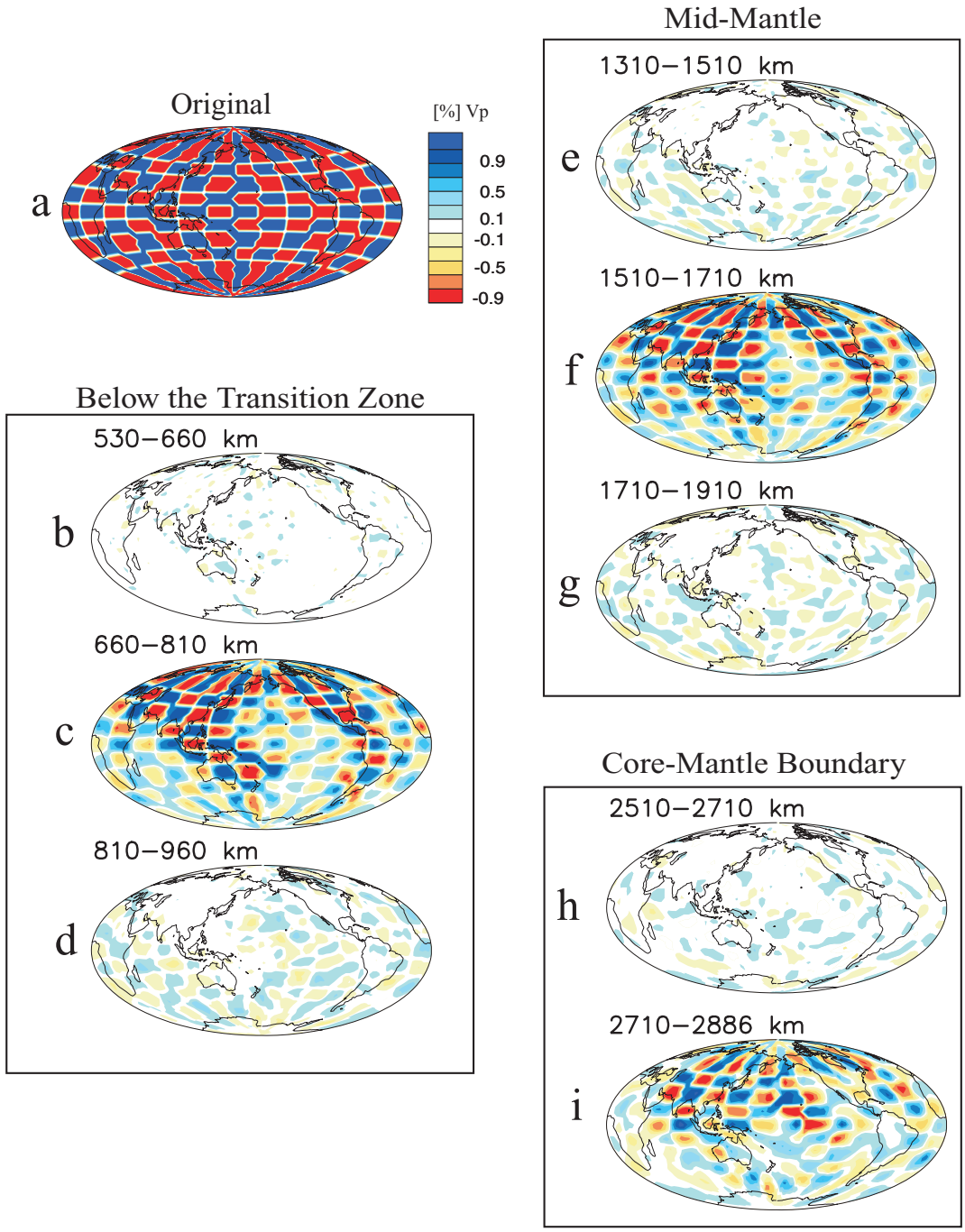

Figure 13. Checkerboard tests (a) applied to our *P* data for layers just below the transition zone (b–d), mid-mantle (e–g) and lowermost mantle (h and i). The checkerboard recovery is similar to that for *S*.

CMB only under the Aleutians. In contrast, we find fast anomalies surrounding the entire Pacific Plate. This discrepancy could be due to the fact that both studies were only able to do their predictions for the last 180 Myr of geological history. The amplitudes of the *P* and *S* velocity anomalies in these fast regions vary with respect to one another as expected for a purely thermal anomaly. This, along with their circum Pacific configuration (in agreement with the last 100 Myr of subduction), indicates that the fast anomalies are most likely the cold remnants of past subduction.

The strongest slow velocity anomalies in the lower mantle are found at the CMB of both our shear and compressional velocity models. They are located in the central Pacific and southern Africa. There is not enough coverage from the *P* data to adequately relate the shear and compressional anomalies for the southern African anomaly. However, the slow anomaly in the central Pacific is much slower for the shear model than the compressional model. Although our resolution decreases at the CMB, a higher magnitude shear anomaly is required by the data. Our results are supported by the

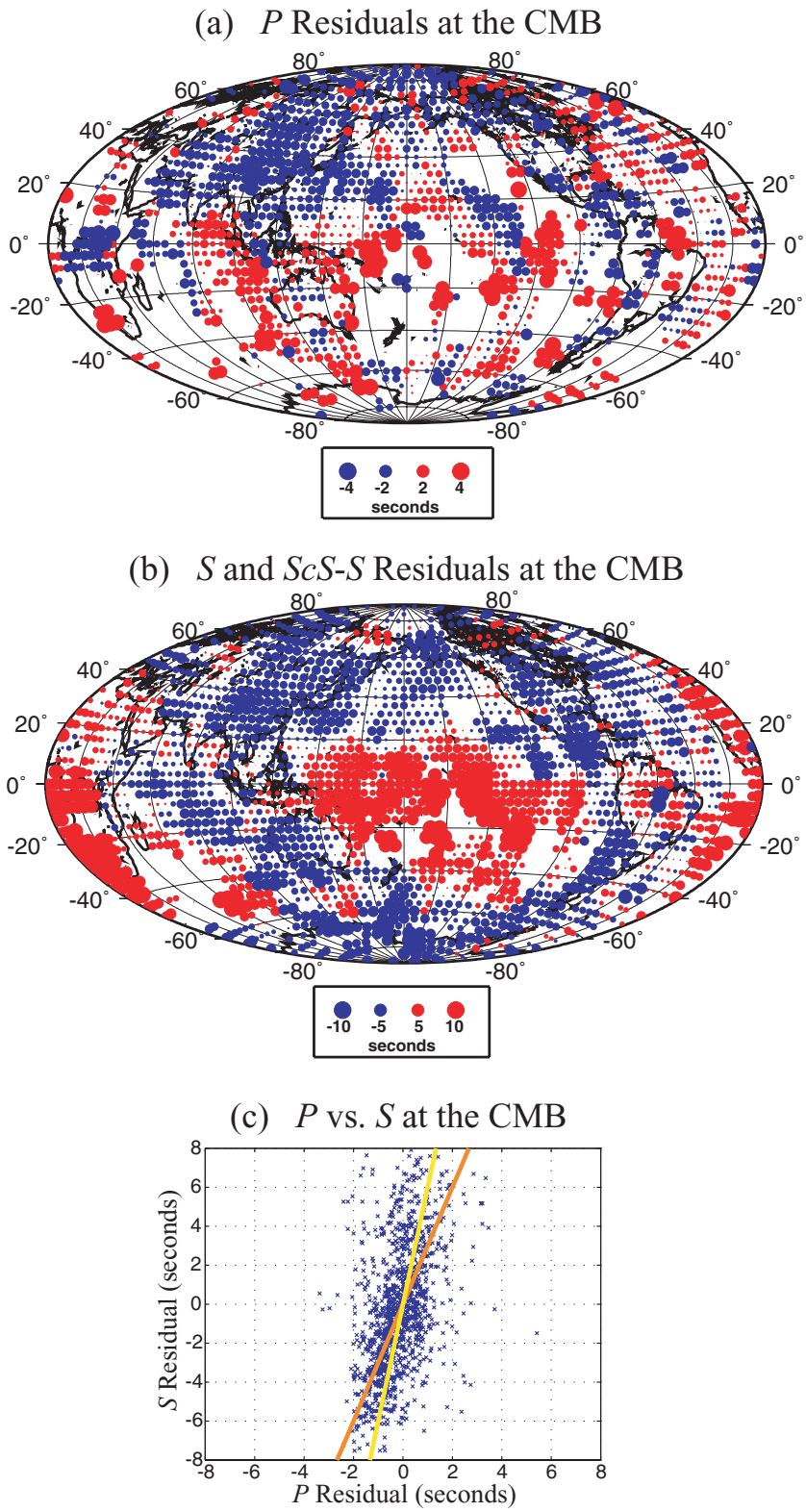

Figure 14. Bin-averaged residuals of our *P* (a) and our combined *S* and *ScS–S* (b) data plotted at their turning points for rays which turn below 2700 km. Note that the pattern is similar, but the *S* and *ScS–S* data provide almost global coverage. In the bottom graph (c) are the residuals of *P* and *S* plotted against each other for co-located bins. The orange line has a slope of 3 which fits the mid-mantle data, and the yellow line has a slope of 6 which better describes the data near the core–mantle boundary (CMB).

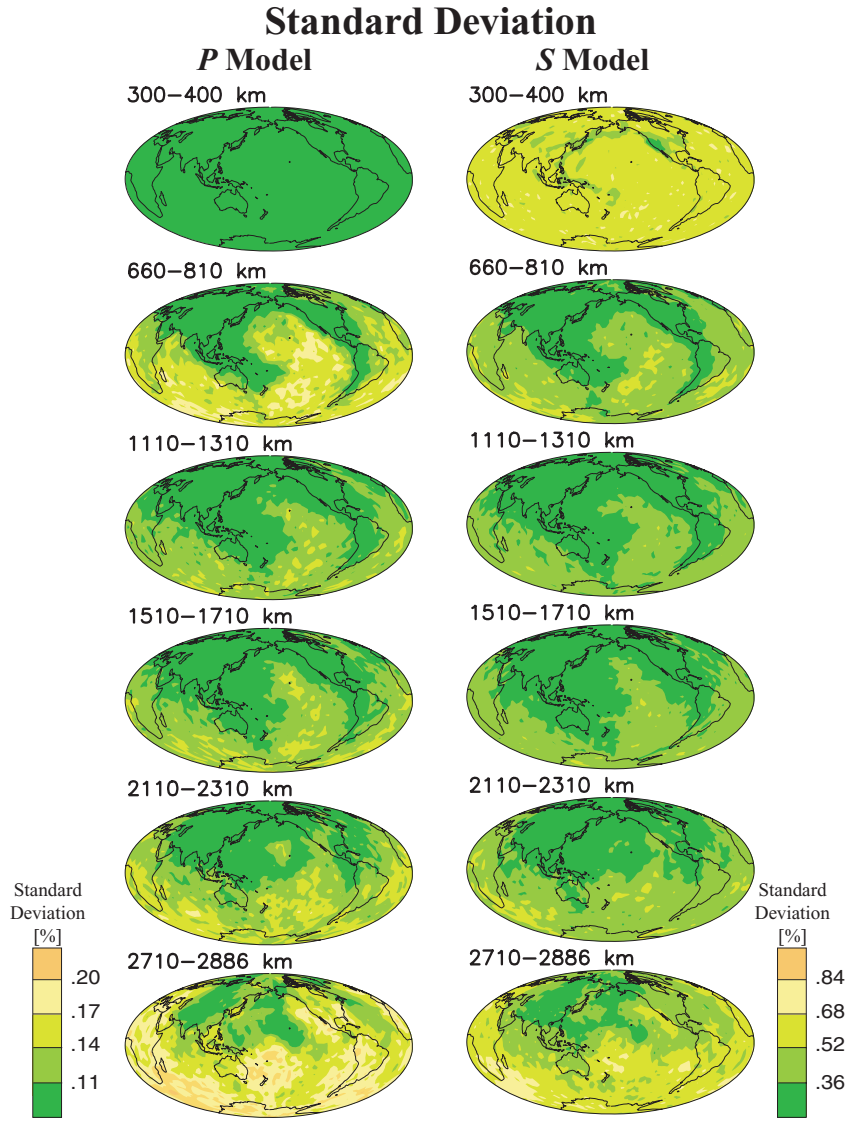

Figure 15. Depth slices of the standard deviation of the velocity anomalies at that depth for the compressional model pictured in Fig. 11 (left-hand side) and the shear model pictured in Fig. 8 (right-hand side). The green areas are well constrained and the orange areas are those that are prone to larger error.

preliminary work of Manners *et al.* (2005), which has greater CMB coverage by applying the cluster analysis method to *S* and *P* waves diffracted around the CMB. The resulting large values of $R = \partial \ln v_s / \partial \ln v_p$ exceed that expected for purely thermal anomalies (Karato & Karki 2001).

Another measure of the likelihood of chemical heterogeneity is the comparison of bulk sound speed and shear velocity anomalies. Using our *P* and *S* data and the fact that the bulk sound speed (V_Φ) is related to shear and compressional velocity by $V_\Phi^2 = V_p^2 - (4/3)V_s^2$, we reframe the inversion to jointly solve for shear velocity and bulk sound speed anomalies. This method is more robust than calculating a bulk sound speed model from a shear and compressional velocity model (Masters *et al.* 2000). Analogous to constructing the compressional model, the bulk model is constrained to the shear model in the upper mantle. Variations in bulk sound speed and shear velocity reflect changes in the bulk and shear modulus, respectively. Fig. 16 demonstrates that the bulk sound speed anomalies are positive whereas the shear velocity anomalies are negative in the vicinity of the CMB. Therefore, the ratio of the two, $\xi = \partial \ln v_s / \partial \ln v_\Phi$, is negative in these regions, which is not possible for a thermal anomaly (Karato & Karki 2001). The anticorrelation is required by the data and not an artefact of sparse coverage. These observations indicate that the shear anomalies in the central Pacific and southern Africa near the CMB likely are both thermal and chemical in origin.

ACKNOWLEDGMENTS

This research was supported by the Institute of Geophysics and Planetary Physics mini-grant program and the National Science Foundation grants NSF EAR01-12289 and NSF EAR05-38238. We thank G. Nolet and J. Ritsema for helpful reviews that improved the manuscript. The velocity models can be downloaded from the corresponding author's website. The data were acquired using the IRIS

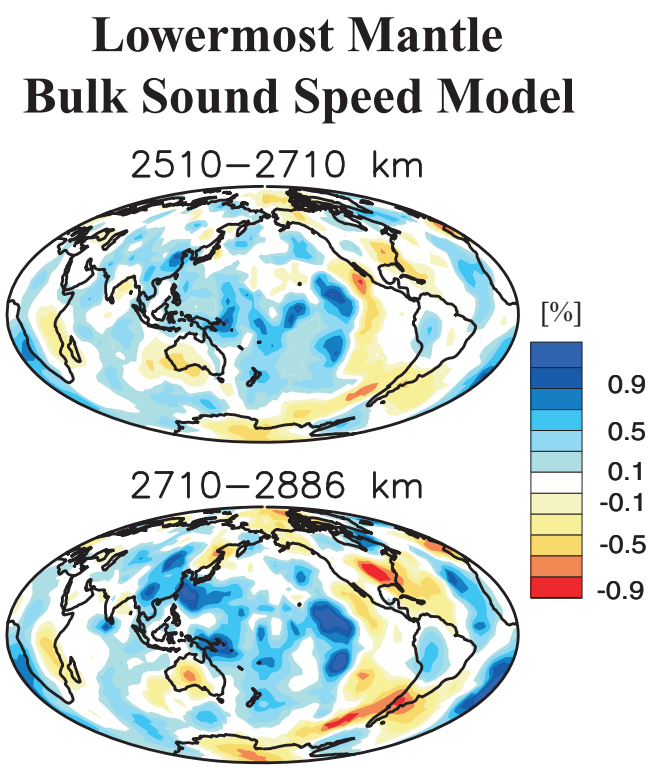

Figure 16. The bottom depth slices of our bulk sound speed model from our joint shear velocity/bulk sound speed inversion. Dark red and blue areas represent anomalies that are 1 per cent slow and fast, respectively. The fast regions beneath the central Pacific and Africa are anticorrelated with the shear velocity anomalies in these areas.

Data Management Center, which is funded through the Instrumentation and Facilities Program of the NSF EAR-0004370. Specific networks include, but are not limited to, GEOSCOPE, IDA, MEDNET, GEOFON, PACIFIC21, and those from the USGS.

REFERENCES

Antolik, M., Gu, Y., Ekstrom, G. & Dziewonski, A., 2003. J362D28: a new joint model of compressional and shear velocity in the Earth's mantle, *Geophys. J. Int.,* **153,** 443–466.

Bassin, G., Laske, G. & Masters, G., 2000. The current limits of resolution for surface wave tomography in North America, *EOS, Trans. Am. geophys. Un.,* **81,** 897.

Beghein, C., Resovsky, J. & Trampert, J., 2002. *P* and *S* tomography using normal-mode and surface waves data with a neighbourhood algorithm, *Geophys. J. Int.,* **149,** 646–658.

Bolton, H., 1996. *Long Period Travel Times and the Structure of the Mantle*, 204 pp., University of California San Diego, La Jolla, CA.

Bolton, H. & Masters, G., 2001. Travel times of *P* and *S* from the global digital networks: implications for the relative variation of *P* and *S* in the mantle, *J. geophys. Res.,* **106,** 13 527–13 540.

Dziewonski, A. & Anderson, D., 1981. Preliminary reference Earth model, *Phys. Earth planet. Inter.,* **25,** 297–356.

Dziewonski, A., Hager, B. & O'Connell, R., 1977. Large-scale heterogeneities in the lower mantle, *J. geophys. Res.,* **82,** 239–255.

Fukao, Y., Widiyantoro, S. & Obayashi, M., 2001. Stagnant slabs in the upper and lower mantle transition region, *Rev. Geophys.,* **39,** 291–323.

Grand, S., 1994. Mantle shear structure beneath the Americas and surrounding oceans, *J. geophys. Res.,* **99,** 11 591–11 621.

Hartigan, J., 1975. Clustering Algorithms, 351 pp., John Wiley & Sons, Inc., New York..

Ishii, M. & Tromp, J., 2004. Constraining large-scale mantle heterogeneity using mantle and inner-core sensitive normal modes, *Phys. Earth planet. Inter.,* **146,** 113–124.

Karason, H. & van der Hilst, R., 2001. Tomographic imaging if the lowermost mantle with differential times of refracted and diffracted core phases (*PKP*, *Pdiff), J. geophys. Res.,* **106,** 6569–6587.

Karato, S., 1993. Importance of anelasticity in the interpretation of seismic tomography, *Geophys. Res. Lett.,* **20,** 1623–1626.

Karato, S. & Karki, B., 2001. Origin of lateral variation of seismic wave velocities and density in the deep mantle, *J. geophys. Res.,* **106,** 21 771–21 783.

Kennett, B., Engdahl, E.R. & Buland, R., 1995. Constraints on seismic velocities in the Earth from travel times, *Geophys. J. Int.,* **122,** 108–124.

Komatitsch, D., Ritsema, J. & Tromp, J., 2002. The spectral-element method, Beowulf computing, and global seismology, *Science,* **298,** 1737–1741.

Lithgow-Bertelloni, C. & Richards, M.A., 1998. Dynamics of Cenozoic and Mesozoic plate motions, *Rev. Geophys.,* **36,** 27–78.

Machetel, P. & Weber, P., 1991. Intermittent layered convection in a mantle model with an endothermic phase change at 670 km, *Nature,* **350,** 55–57.

Manners, U., Reif, C. & Masters, G., 2005. A new method for constraining bulk sound speed at the base of the mantle, *EOS, Trans. Am. geophys. Un.,* **86**(52), 1007.

Masters, G., Johnson, S., Laske, G. & Bolton, H., 1996. A shear-velocity model of the mantle, *Phil. Trans. R. Soc. Lond. A.,* **354,** 1385–1411.

Masters, G., Laske, G., Bolton, H. & Dziewonski, A., 2000. The relative behaviour of shear velocity, bulk sound speed, and compressional velocity in the mantle: implications for chemical and thermal structure, in *Earth's Deep Interior: Mineral Physics and Tomography from the Atomic to Global Scale*, pp. 63–87, American Geophysical Union.

Megnin, C. & Romanowicz, B., 2000. The three-dimensional shear velocity structure of the mantle from the inversion of body, surface and higher-mode waveforms, *Geophys. J. Int.,* **143,** 709–728.

Montelli, R., Nolet, G., Masters, G., Dahlen, F. & Hung, S.-H., 2004a, Global *P* and *PP* traveltime tomography: rays versus waves, *Geophys. J. Int.,* **158,** 637–654.

Montelli, R., Nolet, G., Dahlen, F., Masters, G., Engdahl, E.R. & Hung, S.H., 2004b, Finite-frequency tomography reveals a variety of plumes in the mantle, *Science,* **303,** 338–343.

Paige, C. & Saunders, M., 1973. Solution of sparse indefinite systems of equations and least-squares problems, Res. Rep. STAN-CS-73-399, Stanford University, Stanford, CA.

Reif, C., Masters, G., Shearer, P. & Laske, G., 2002. Cluster analysis of long-period waveforms: Implications for global tomography, *EOS, Trans. Am. geophys. Un.,* **83**(47), p. 954.

Ricard, Y., Richards, M., Lithgow-Bertelloni, C. & Stunff, Y.L., 1993. A geodynamic model of mantle density heterogeneity, *J. geophys. Res.,* **98,** 21 895–21 910.

Ritsema, J. & van Heijst, H., 2002. Constraints on the correlation of *P*- and *S*-wave velocity heterogeneity in the mantle from *P*, *PP, PPP,* and *PKPab* traveltimes, *Geophys. J. Int.,* **149,** 482–489.

Robertson, G. & Woodhouse, J., 1995. Evidence for proportionality of *P* and *S* heterogeneity in the lower mantle, *Geophys. J. Int.,* **123,** 85–116.

Robertson, G. & Woodhouse, J., 1996. Ratio of relative *S* to *P* velocity heterogeneity in the lower mantle, *J. geophys. Res.,* **101,** 20 041–20 052.

Romanowicz, B., 2003. Global mantle tomography: progress status in the past 10 years, *Ann. Rev. Earth planet. Sci.,* **31,** 303–328.

Rost, S. & Thomas, C., 2002. Array seismology: Methods and application, *Rev. Geophys.,* **40,** doi:10.1029/2000RG000100.

Rowe, C.A., Aster, R.C., Borchhers, B. & Young, C.J., 2002. An automatic, adaptive algorithm for refining phase picks in large seismic data sets, *Bull. seism. Soc. Am.,* **92,** 1660–1674. doi:10.1785/0120010224.

Saltzer, R., van der Hilst, R. & Karason, H., 2001. Comparing *P* and *S* wave heterogeneity in the mantle, *Geophys. Res. Lett.,* **28,** 1335–1338.

Schubert, G., Masters, G., Olson, P. & Tackley, P., 2004. Superplumes or plume clusters? *Phys. Earth planet. Inter.,* **146,** 147–162.

Sigloch, K. & Nolet, G., 2006. Measuring finite-frequency body wave amplitudes and traveltimes, *Geophys. J. Int.,* **167,** 271–287.

Simmons, N.A., Forte, A.M. & Grand, S.P., 2006. Constraining mantle flow with seismic and geodynamic data: a joint approach, *Earth planet. Sci. Lett.,* **246,** 109–124.

Su, W. & Dziewonski, A., 1997. Simultaneous inversion for 3D variations in shear and bulk velocity in the mantle, *Phys. Earth planet. Inter.,* **100,** 135–156.

Tan, E. & Gurnis, M., 2002. Slabs in the lower mantle and their modulation of plume formation, *Geochem. Geophys. Geosyst.,* **3,** doi:10.1029/2001GC000238.

VanDecar, J. & Crosson, R., 1990. Determination of teleseismic relative phase arrival times using multi-channel cross-correlation and least squares., *Bull. seism. Soc. Am.,* **80,** 150–169.

van der Hilst, R. & Karason, H., 1999. Compositional heterogeneity in the bottom 1000 kilometers of the Earth's mantle: toward a hybrid convection model, *Science,* **283,** 1885–1888.

van der Hilst, R., Widiyantoro, S. & Engdahl, E.R., 1997. Evidence for deep mantle circulation from global tomography, *Nature,* **386,** 578–584.

Van der Voo, R., Spakman, W. & Bijwaard, H., 1999. Tethyan subducted slabs under India, *Earth planet. Sci. Lett.,* **171,** 7–20.

Woodward, R. & Masters, G., 1991a, Global upper mantle structure from long-period differential travel times, *J. geophys. Res.,* **96,** 6351–6377.

Woodward, R. & Masters, G., 1991b, Lower mantle structure from *ScS-S* differential travel times, *Nature,* **352,** 231–233.